Low-mass vector-meson production at forward rapidity in $p+p$ collisions at $\sqrt{s} = 200$ GeV

A. Adare,[13] C. Aidala,[38,43] N. N. Ajitanand,[61] Y. Akiba,[55,56] R. Akimoto,[12] H. Al-Ta'ani,[49] J. Alexander,[61] M. Alfred,[23] K. R. Andrews,[1] A. Angerami,[14] K. Aoki,[55] N. Apadula,[28,62] E. Appelt,[66] Y. Aramaki,[12,55] R. Armendariz,[8] H. Asano,[34,55] E. C. Aschenauer,[7] E. T. Atomssa,[62] T. C. Awes,[51] B. Azmoun,[7] V. Babintsev,[24] M. Bai,[6] N. S. Bandara,[42] B. Bannier,[62] K. N. Barish,[8] B. Bassalleck,[48] A. T. Basye,[1] S. Bathe,[5,56] V. Baublis,[54] C. Baumann,[44] A. Bazilevsky,[7] M. Beaumier,[8] S. Beckman,[13] R. Belmont,[43,66] J. Ben-Benjamin,[45] R. Bennett,[62] A. Berdnikov,[58] Y. Berdnikov,[58] D. Black,[8] D. S. Blau,[33] J. Bok,[49] J. S. Bok,[69] K. Boyle,[56] M. L. Brooks,[38] D. Broxmeyer,[45] J. Bryslawskyj,[5] H. Buesching,[7] V. Bumazhnov,[24] G. Bunce,[7,56] S. Butsyk,[38] S. Campbell,[28,62] P. Castera,[62] C.-H. Chen,[56,62] C. Y. Chi,[14] M. Chiu,[7] I. J. Choi,[25,69] J. B. Choi,[10] R. K. Choudhury,[4] P. Christiansen,[40] T. Chujo,[65] O. Chvala,[8] V. Cianciolo,[51] Z. Citron,[62,67] B. A. Cole,[14] Z. Conesa del Valle,[35] M. Connors,[62] M. Csanád,[17] T. Csörgő,[68] S. Dairaku,[34,55] A. Datta,[42,48] M. S. Daugherity,[1] G. David,[7] M. K. Dayananda,[20] K. DeBlasio,[48] K. Dehmelt,[62] A. Denisov,[24] A. Deshpande,[56,62] E. J. Desmond,[7] K. V. Dharmawardane,[49] O. Dietzsch,[59] L. Ding,[28] A. Dion,[28,62] J. H. Do,[69] M. Donadelli,[59] O. Drapier,[35] A. Drees,[62] K. A. Drees,[6] J. M. Durham,[38,62] A. Durum,[24] L. D'Orazio,[41] Y. V. Efremenko,[51] T. Engelmore,[14] A. Enokizono,[51,55,57] H. En'yo,[55,56] S. Esumi,[65] B. Fadem,[45] N. Feege,[62] D. E. Fields,[48] M. Finger,[9] M. Finger, Jr.,[9] F. Fleuret,[35] S. L. Fokin,[33] J. E. Frantz,[50] A. Franz,[7] A. D. Frawley,[19] Y. Fukao,[55] T. Fusayasu,[47] C. Gal,[62] P. Gallus,[15] P. Garg,[3] I. Garishvili,[63] H. Ge,[62] F. Giordano,[25] A. Glenn,[37] X. Gong,[61] M. Gonin,[35] Y. Goto,[55,56] R. Granier de Cassagnac,[35] N. Grau,[2,14] S. V. Greene,[66] M. Grosse Perdekamp,[25] Y. Gu,[61] T. Gunji,[12] L. Guo,[38] H. Guragain,[20] H.-Å. Gustafsson,[40,*] T. Hachiya,[55] J. S. Haggerty,[7] K. I. Hahn,[18] H. Hamagaki,[12] J. Hamblen,[63] R. Han,[53] S. Y. Han,[18] J. Hanks,[14,62] C. Harper,[45] S. Hasegawa,[29] K. Hashimoto,[55,57] E. Haslum,[40] R. Hayano,[12] X. He,[20] T. K. Hemmick,[62] T. Hester,[8] J. C. Hill,[28] R. S. Hollis,[8] W. Holzmann,[14] K. Homma,[22] B. Hong,[32] T. Horaguchi,[65] Y. Hori,[12] D. Hornback,[51] T. Hoshino,[22] S. Huang,[66] T. Ichihara,[55,56] R. Ichimiya,[55] H. Iinuma,[31] Y. Ikeda,[55,65] K. Imai,[29,34,55] Y. Imazu,[55] M. Inaba,[65] A. Iordanova,[8] D. Isenhower,[1] M. Ishihara,[55] M. Issah,[66] D. Ivanischev,[54] D. Ivanishchev,[54] Y. Iwanaga,[22] B. V. Jacak,[62] S. J. Jeon,[46] M. Jezghani,[20] J. Jia,[7,61] X. Jiang,[38] D. John,[63] B. M. Johnson,[7] T. Jones,[1] E. Joo,[32] K. S. Joo,[46] D. Jouan,[52] D. S. Jumper,[25] J. Kamin,[62] S. Kaneti,[62] B. H. Kang,[21] J. H. Kang,[69] J. S. Kang,[21] J. Kapustinsky,[38] K. Karatsu,[34,55] M. Kasai,[55,57] D. Kawall,[42,56] A. V. Kazantsev,[33] T. Kempel,[28] J. A. Key,[48] V. Khachatryan,[62] A. Khanzadeev,[54] K. Kihara,[65] K. M. Kijima,[22] B. I. Kim,[32] C. Kim,[32] D. H. Kim,[18] D. J. Kim,[30] E.-J. Kim,[10] H.-J. Kim,[69] M. Kim,[60] Y.-J. Kim,[25] Y. K. Kim,[21] E. Kinney,[13] Á. Kiss,[17] E. Kistenev,[7] J. Klatsky,[19] D. Kleinjan,[8] P. Kline,[62] T. Koblesky,[13] L. Kochenda,[54] M. Kofarago,[17] B. Komkov,[54] M. Konno,[65] J. Koster,[25,56] D. Kotov,[54,58] A. Král,[15] G. J. Kunde,[38] K. Kurita,[55,57] M. Kurosawa,[55,56] Y. Kwon,[69] G. S. Kyle,[49] R. Lacey,[61] Y. S. Lai,[14] J. G. Lajoie,[28] A. Lebedev,[28] D. M. Lee,[38] J. Lee,[18] K. B. Lee,[32,38] K. S. Lee,[32] S. H. Lee,[62] S. R. Lee,[10] M. J. Leitch,[38] M. A. L. Leite,[59] M. Leitgab,[25] X. Li,[11] S. H. Lim,[69] L. A. Linden Levy,[13] H. Liu,[38] M. X. Liu,[38] B. Love,[66] D. Lynch,[7] C. F. Maguire,[66] Y. I. Makdisi,[6] M. Makek,[67,70] A. Manion,[62] V. I. Manko,[33] E. Mannel,[7,14] Y. Mao,[53,55] H. Masui,[65] M. McCumber,[13,38,62] P. L. McGaughey,[38] D. McGlinchey,[13,19] C. McKinney,[25] N. Means,[62] A. Meles,[49] M. Mendoza,[8] B. Meredith,[14,25] Y. Miake,[65] T. Mibe,[31] A. C. Mignerey,[41] K. Miki,[55,65] A. J. Miller,[1] A. Milov,[67] D. K. Mishra,[4] J. T. Mitchell,[7] Y. Miyachi,[55,64] S. Miyasaka,[55,64] S. Mizuno,[55,65] A. K. Mohanty,[4] P. Montuenga,[25] H. J. Moon,[46] T. Moon,[69] Y. Morino,[12] A. Morreale,[8] D. P. Morrison,[7,†] S. Motschwiller,[45] T. V. Moukhanova,[33] T. Murakami,[34,55] J. Murata,[55,57] A. Mwai,[61] S. Nagamiya,[31,55] J. L. Nagle,[13,‡] M. Naglis,[67] M. I. Nagy,[17,68] I. Nakagawa,[55,56] H. Nakagomi,[55,65] Y. Nakamiya,[22] K. R. Nakamura,[34,55] T. Nakamura,[55] K. Nakano,[55,64] C. Nattrass,[63] P. K. Netrakanti,[4] J. Newby,[37] M. Nguyen,[62] M. Nihashi,[22,55] T. Niida,[65] R. Nouicer,[7,56] N. Novitzky,[30] A. S. Nyanin,[33] C. Oakley,[20] E. O'Brien,[7] C. A. Ogilvie,[28] M. Oka,[65] K. Okada,[56] J. D. Orjuela Koop,[13] A. Oskarsson,[40] M. Ouchida,[22,55] H. Ozaki,[65] K. Ozawa,[12,31] R. Pak,[7] V. Pantuev,[26,62] V. Papavassiliou,[49] B. H. Park,[21] I. H. Park,[18] S. Park,[60] S. K. Park,[32] S. F. Pate,[49] L. Patel,[20] M. Patel,[28] H. Pei,[28] J.-C. Peng,[25] H. Pereira,[16] D. V. Perepelitsa,[7,14] G. D. N. Perera,[49] D. Yu. Peressounko,[33] J. Perry,[28] R. Petti,[62] C. Pinkenburg,[7] R. Pinson,[1] R. P. Pisani,[7] M. Proissl,[62] M. L. Purschke,[7] H. Qu,[20] J. Rak,[30] I. Ravinovich,[67] K. F. Read,[51,63] K. Reygers,[44] D. Reynolds,[61] V. Riabov,[54] Y. Riabov,[54,58] E. Richardson,[41] N. Riveli,[50] D. Roach,[66] G. Roche,[39] S. D. Rolnick,[8] M. Rosati,[28] S. S. E. Rosendahl,[40] Z. Rowan,[5] J. G. Rubin,[43] B. Sahlmueller,[44,62] N. Saito,[31] T. Sakaguchi,[7] H. Sako,[29] V. Samsonov,[54] S. Sano,[12] M. Sarsour,[20] S. Sato,[29] T. Sato,[65] M. Savastio,[62] S. Sawada,[31] B. Schaefer,[66] B. K. Schmoll,[63] K. Sedgwick,[8] J. Seele,[56] R. Seidl,[55,56] A. Sen,[63] R. Seto,[8] P. Sett,[4] A. Sexton,[41] D. Sharma,[62,67] I. Shein,[24] T.-A. Shibata,[55,64] K. Shigaki,[22] H. H. Shim,[32] M. Shimomura,[28,65] K. Shoji,[34,55] P. Shukla,[4] A. Sickles,[7] C. L. Silva,[28,38] D. Silvermyr,[51] C. Silvestre,[16] K. S. Sim,[32] B. K. Singh,[3] C. P. Singh,[3] V. Singh,[3] M. Slunečka,[9] T. Sodre,[45] R. A. Soltz,[37] W. E. Sondheim,[38] S. P. Sorensen,[63] I. V. Sourikova,[7] P. W. Stankus,[51] E. Stenlund,[40] M. Stepanov,[42] S. P. Stoll,[7] T. Sugitate,[22] A. Sukhanov,[7] T. Sumita,[55] J. Sun,[62] J. Sziklai,[68] E. M. Takagui,[59] A. Takahara,[12] A. Taketani,[55,56] R. Tanabe,[65] Y. Tanaka,[47] S. Taneja,[62] K. Tanida,[34,55,56,60] M. J. Tannenbaum,[7] S. Tarafdar,[3,67] A. Taranenko,[61] E. Tennant,[49] H. Themann,[62] D. Thomas,[1] R. Tieulent,[20] A. Timilsina,[28] T. Todoroki,[55,65] M. Togawa,[56] L. Tomášek,[27] M. Tomášek,[15,27] H. Torii,[22,55] M. Towell,[1] R. Towell,[1] R. S. Towell,[1] I. Tserruya,[67] Y. Tsuchimoto,[22] K. Utsunomiya,[12] C. Vale,[7] H. W. van Hecke,[38] M. Vargyas,[68] E. Vazquez-Zambrano,[14]

A. Veicht,[14] J. Velkovska,[66] R. Vértesi,[68] M. Virius,[15] A. Vossen,[25] V. Vrba,[15,27] E. Vznuzdaev,[54] X. R. Wang,[49] D. Watanabe,[22] K. Watanabe,[65] Y. Watanabe,[55,56] Y. S. Watanabe,[12,31] F. Wei,[28,49] R. Wei,[61] J. Wessels,[44] S. Whitaker,[28] S. N. White,[7] D. Winter,[14] S. Wolin,[25] C. L. Woody,[7] R. M. Wright,[1] M. Wysocki,[13,51] B. Xia,[50] L. Xue,[20] S. Yalcin,[62] Y. L. Yamaguchi,[12,55] R. Yang,[25] A. Yanovich,[24] J. Ying,[20] S. Yokkaichi,[55,56] J. S. Yoo,[18] I. Yoon,[60] Z. You,[38,53] G. R. Young,[51] I. Younus,[36,48] I. E. Yushmanov,[33] W. A. Zajc,[14] A. Zelenski,[6] and S. Zhou[11]

(PHENIX Collaboration)

[1]*Abilene Christian University, Abilene, Texas 79699, USA*
[2]*Department of Physics, Augustana College, Sioux Falls, South Dakota 57197, USA*
[3]*Department of Physics, Banaras Hindu University, Varanasi 221005, India*
[4]*Bhabha Atomic Research Centre, Bombay 400 085, India*
[5]*Baruch College, City University of New York, New York, New York 10010, USA*
[6]*Collider-Accelerator Department, Brookhaven National Laboratory, Upton, New York 11973-5000, USA*
[7]*Physics Department, Brookhaven National Laboratory, Upton, New York 11973-5000, USA*
[8]*University of California–Riverside, Riverside, California 92521, USA*
[9]*Charles University, Ovocný trh 5, Praha 1, 116 36 Prague, Czech Republic*
[10]*Chonbuk National University, Jeonju 561-756, Korea*
[11]*Science and Technology on Nuclear Data Laboratory, China Institute of Atomic Energy, Beijing 102413, People's Republic of China*
[12]*Center for Nuclear Study, Graduate School of Science, University of Tokyo, 7-3-1 Hongo, Bunkyo, Tokyo 113-0033, Japan*
[13]*University of Colorado, Boulder, Colorado 80309, USA*
[14]*Columbia University, New York, New York 10027 and Nevis Laboratories, Irvington, New York 10533, USA*
[15]*Czech Technical University, Zikova 4, 166 36 Prague 6, Czech Republic*
[16]*Dapnia, CEA Saclay, F-91191 Gif-sur-Yvette, France*
[17]*ELTE, Eötvös Loránd University, H-1117 Budapest, Pázmány P. s. 1/A, Hungary*
[18]*Ewha Womans University, Seoul 120-750, Korea*
[19]*Florida State University, Tallahassee, Florida 32306, USA*
[20]*Georgia State University, Atlanta, Georgia 30303, USA*
[21]*Hanyang University, Seoul 133-792, Korea*
[22]*Hiroshima University, Kagamiyama, Higashi-Hiroshima 739-8526, Japan*
[23]*Department of Physics and Astronomy, Howard University, Washington, DC 20059, USA*
[24]*IHEP Protvino, State Research Center of Russian Federation, Institute for High Energy Physics, Protvino 142281, Russia*
[25]*University of Illinois at Urbana-Champaign, Urbana, Illinois 61801, USA*
[26]*Institute for Nuclear Research of the Russian Academy of Sciences, prospekt 60-letiya Oktyabrya 7a, Moscow 117312, Russia*
[27]*Institute of Physics, Academy of Sciences of the Czech Republic, Na Slovance 2, 182 21 Prague 8, Czech Republic*
[28]*Iowa State University, Ames, Iowa 50011, USA*
[29]*Advanced Science Research Center, Japan Atomic Energy Agency, 2-4 Shirakata Shirane, Tokai-mura, Naka-gun, Ibaraki-ken 319-1195, Japan*
[30]*Helsinki Institute of Physics and University of Jyväskylä, P.O. Box 35, FI-40014 Jyväskylä, Finland*
[31]*KEK, High Energy Accelerator Research Organization, Tsukuba, Ibaraki 305-0801, Japan*
[32]*Korea University, Seoul 136-701, Korea*
[33]*Russian Research Center "Kurchatov Institute", Moscow 123098, Russia*
[34]*Kyoto University, Kyoto 606-8502, Japan*
[35]*Laboratoire Leprince-Ringuet, Ecole Polytechnique, CNRS-IN2P3, Route de Saclay, F-91128 Palaiseau, France*
[36]*Physics Department, Lahore University of Management Sciences, Lahore 54792, Pakistan*
[37]*Lawrence Livermore National Laboratory, Livermore, California 94550, USA*
[38]*Los Alamos National Laboratory, Los Alamos, New Mexico 87545, USA*
[39]*LPC, Université Blaise Pascal, CNRS-IN2P3, Clermont-Fd, 63177 Aubiere Cedex, France*
[40]*Department of Physics, Lund University, P.O. Box 118, SE-221 00 Lund, Sweden*
[41]*University of Maryland, College Park, Maryland 20742, USA*
[42]*Department of Physics, University of Massachusetts, Amherst, Massachusetts 01003-9337, USA*
[43]*Department of Physics, University of Michigan, Ann Arbor, Michigan 48109-1040, USA*
[44]*Institut fur Kernphysik, University of Muenster, D-48149 Muenster, Germany*

[45]Muhlenberg College, Allentown, Pennsylvania 18104-5586, USA
[46]Myongji University, Yongin, Kyonggido 449-728, Korea
[47]Nagasaki Institute of Applied Science, Nagasaki-shi, Nagasaki 851-0193, Japan
[48]University of New Mexico, Albuquerque, New Mexico 87131, USA
[49]New Mexico State University, Las Cruces, New Mexico 88003, USA
[50]Department of Physics and Astronomy, Ohio University, Athens, Ohio 45701, USA
[51]Oak Ridge National Laboratory, Oak Ridge, Tennessee 37831, USA
[52]IPN-Orsay, Universite Paris Sud, CNRS-IN2P3, BP1, F-91406 Orsay, France
[53]Peking University, Beijing 100871, People's Republic of China
[54]PNPI, Petersburg Nuclear Physics Institute, Gatchina, Leningrad region 188300, Russia
[55]RIKEN Nishina Center for Accelerator-Based Science, Wako, Saitama 351-0198, Japan
[56]RIKEN BNL Research Center, Brookhaven National Laboratory, Upton, New York 11973-5000, USA
[57]Physics Department, Rikkyo University, 3-34-1 Nishi-Ikebukuro, Toshima, Tokyo 171-8501, Japan
[58]Saint Petersburg State Polytechnic University, St. Petersburg 195251, Russia
[59]Universidade de São Paulo, Instituto de Física, Caixa Postal 66318, São Paulo CEP05315-970, Brazil
[60]Department of Physics and Astronomy, Seoul National University, Seoul 151-742, Korea
[61]Chemistry Department, Stony Brook University, SUNY, Stony Brook, New York 11794-3400, USA
[62]Department of Physics and Astronomy, Stony Brook University, SUNY, Stony Brook, New York 11794-3800, USA
[63]University of Tennessee, Knoxville, Tennessee 37996, USA
[64]Department of Physics, Tokyo Institute of Technology, Oh-okayama, Meguro, Tokyo 152-8551, Japan
[65]Institute of Physics, University of Tsukuba, Tsukuba, Ibaraki 305, Japan
[66]Vanderbilt University, Nashville, Tennessee 37235, USA
[67]Weizmann Institute, Rehovot 76100, Israel
[68]Institute for Particle and Nuclear Physics, Wigner Research Centre for Physics, Hungarian Academy of Sciences (Wigner RCP, RMKI) H-1525 Budapest 114, P.O. Box 49, Budapest, Hungary
[69]Yonsei University, IPAP, Seoul 120-749, Korea
[70]University of Zagreb, Faculty of Science, Department of Physics, Bijenička 32, HR-10002 Zagreb, Croatia

(Received 23 May 2014; published 8 September 2014)

The PHENIX experiment at the Relativistic Heavy Ion Collider has measured low-mass vector-meson, ω, ρ, and ϕ, production through the dimuon decay channel at forward rapidity ($1.2 < |y| < 2.2$) in $p + p$ collisions at $\sqrt{s} = 200$ GeV. The differential cross sections for these mesons are measured as a function of both p_T and rapidity. We also report the integrated differential cross sections over $1 < p_T < 7$ GeV/c and $1.2 < |y| < 2.2$: $d\sigma/dy(\omega+\rho\to\mu\mu) = 80 \pm 6(\text{stat}) \pm 12(\text{syst})$ nb and $d\sigma/dy(\phi\to\mu\mu) = 27 \pm 3(\text{stat}) \pm 4(\text{syst})$ nb. These results are compared with midrapidity measurements and calculations.

DOI: 10.1103/PhysRevD.90.052002 PACS numbers: 13.20.Jf, 25.75.Dw

I. INTRODUCTION

Low-mass vector-meson (LVM) production in $p + p$ collisions is an important tool to study QCD, providing data to tune phenomenological soft QCD models and to compare to hard perturbative QCD calculations. Various experiments [1–6] have studied LVM at different colliding energies and in different kinematic regions.

In addition, LVM production in $p + p$ collisions provides a reference for high-energy heavy-ion-collision measurements. LVM studies provide key information on the hot and dense state of the strongly interacting matter produced in such collisions. Among them, strangeness enhancement [7], a phenomenon associated with soft particles in bulk matter, can be accessed through the measurements of ϕ-meson production [8–13] and the $\phi/(\rho + \omega)$ ratio. The measurement of the ρ spectral function can be used to reveal in-medium modifications of the hadron properties close to the QCD phase boundary linked to chiral symmetry restoration [14–16]. However, measuring the ρ spectral function in the two-muon channel requires better mass resolution than is provided by the muon spectrometers of the PHENIX experiment at the Relativistic Heavy Ion Collider.

Having two muon spectrometers covering the rapidity range $1.2 < |y| < 2.2$, PHENIX is able to study vector-meson production via the dimuon decay channel. Because

*Deceased
†PHENIX Co-Spokesperson. morrison@bnl.gov
‡PHENIX Co-Spokesperson. jamie.nagle@colorado.edu

there is no similar measurement in this kinematic regime at this energy, the forward rapidity measurements are a valuable addition to the database and are complementary to previously published midrapidity results [1,2]. We report the differential cross section as a function of p_T and rapidity of $(\omega+\rho)$ and ϕ mesons for $1 < p_T < 7\ \mathrm{GeV}/c$ and $1.2 < |y| < 2.2$. Results presented in this paper are based on the data sample collected in 2009 using the PHENIX muon spectrometers in $p+p$ collisions at $\sqrt{s} = 200$ GeV. The sampled luminosity of the data used in this analysis corresponds to 14.1 pb^{-1}.

II. EXPERIMENT

The PHENIX apparatus is described in detail in Ref. [17]. This analysis uses the dimuon decay channel of the low-mass vector mesons. The detectors relevant for reconstruction and triggering are the two muon spectrometers [18] and the two beam-beam counters (BBCs) in the forward and backward rapidities.

The muon spectrometers, located behind an absorber composed of 19 cm copper and 60 cm iron, include the muon tracker (MuTr), which is in a radial magnetic field with an integrated bending power of 0.8 Tesla-meter, followed by the muon identifier (MuID). The muon spectrometers cover the range $1.2 < |\eta| < 2.2$ over the full azimuth. The MuTr comprises three sets of cathode strip chambers while the MuID comprises five planes of Iarocci tubes interleaved with steel absorber plates. The composite momentum resolution, $\delta p/p$, of particles in the analyzed momentum range is about 5%, independent of momentum and dominated by multiple scattering. The LVM mass resolution is 85 MeV/c^2. Muon candidates are identified by reconstructed tracks in the MuTr matched to MuID tracks that penetrate through to the last MuID plane. The minimum momentum of a muon to reach the last MuID plane is $\sim 2\ \mathrm{GeV}/c$.

The BBC, comprising two arrays of 64 Čerenkov counters covering the pseudorapidity range $3.1 < |\eta| < 3.9$, were used to measure the collision vertex along the beam axis (z_{vtx}) with 2-cm resolution in addition to providing a minimum-bias (MB) trigger.

III. DATA ANALYSIS

The data set for this analysis was recorded in 2009 using a MB trigger that required at least one hit in each of the BBCs. Additionally, the MuID Level-1 dimuon trigger was used which required that at least two tracks penetrate through the MuID to its last layer.

A set of quality assurance cuts is applied to the data to select good muon candidates and improve the signal-to-background ratio. The BBC collision z vertex is required to be within ± 30 cm of the center of the interaction region along the beam direction. The MuTr tracks are matched to the MuID tracks at the first MuID layer in both position and angle. In addition, the track trajectory is required to have at least 8 of 10 possible hits in the MuID.

The invariant mass distribution is formed by combining muon candidate tracks of opposite charge. In addition to low-mass vector mesons, the invariant mass spectra contain uncorrelated and correlated backgrounds. The uncorrelated backgrounds arise from random combinatoric associations of unrelated muon candidates while the correlated backgrounds arise from open charm decay (e.g., $D\bar{D}$ where both decay semileptonically to muons), open bottom decay, η and ω Dalitz decays and the Drell-Yan process. The correlated heavy-flavor background is small (see Sec. IV).

Traditionally, the uncorrelated background is estimated and subtracted by two methods. The first method uses the mass spectra of the like-sign pairs that are reconstructed within the same event. The other forms unlike-sign and like-sign pairs from different events and is often referred to as the "mixed-event method." In the like-sign method, the like-sign pairs are expected to originate from combinatorial processes; in addition there can be correlated pairs within a single event [19]. In the case of the mixed-event method, unlike-sign pairs are formed from tracks from different events which provide purely combinatorial pairs [19,20]. The results of using these two methods are shown in Fig. 1.

It is clear from Fig. 1 that the two methods are not able to reproduce the background in the low-mass region. Hence, we introduce a new data-driven technique to extract the background in the low-mass region.

It was established from simulation that the background in the low-mass region is dominated by 1) $K/\pi \to \mu^{+/-}$ decays that occur before reaching the absorber, 2) punch-through hadrons with high p_T that are misidentified as muons and 3) muons that result from decays in the muon tracker volume. The track pairs from these backgrounds produce a broader distribution of χ^2_{vtx} which allows the subtraction of these backgrounds utilizing the χ^2_{vtx} variable.

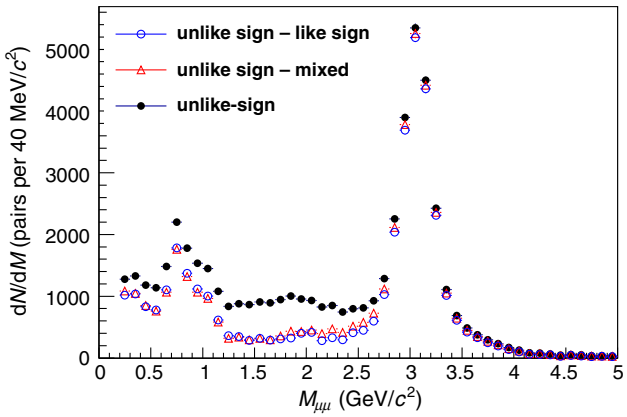

FIG. 1 (color online). The unlike-sign dimuon invariant mass spectra before background subtraction (solid black points), after subtracting mixed-events background (empty red triangles) and after subtracting like-sign background (empty blue circles).

The $\chi^2_{\rm vtx}$ is the result of a simultaneous fit of the two muon tracks with a common vertex that comes from the BBC measured event vertex position. This procedure separates the foreground and background spectra by applying a cut of $\chi^2_{\rm vtx} < 3.6$ to extract foreground spectra and a cut of $\chi^2_{\rm vtx} > 3.6$ to extract background spectra. The value, $\chi^2_{\rm vtx,cut} = 3.6$, was selected such that we retain as much of the signal as possible while still allowing enough statistics in our background sample.

Figure 2(a) shows the unlike-sign pairs $\chi^2_{\rm vtx}$ distribution, which is narrower in the resonance region dominated by prompt dimuons (e.g., in the J/ψ region, $2.5 < M_{\mu^+\mu^-} < 3.7$ GeV/c^2), and wider in the nonresonance regions. However, the $\chi^2_{\rm vtx}$ distribution for the like-sign pairs is the same in both mass regions. In addition, the unlike-sign $\chi^2_{\rm vtx}$ distribution agrees very well with that of the like-sign in the nonresonance region. These observations help support the hypothesis that higher-valued $\chi^2_{\rm vtx}$ entries in both the unlike-sign and like-sign spectra are coming primarily from hadronic backgrounds.

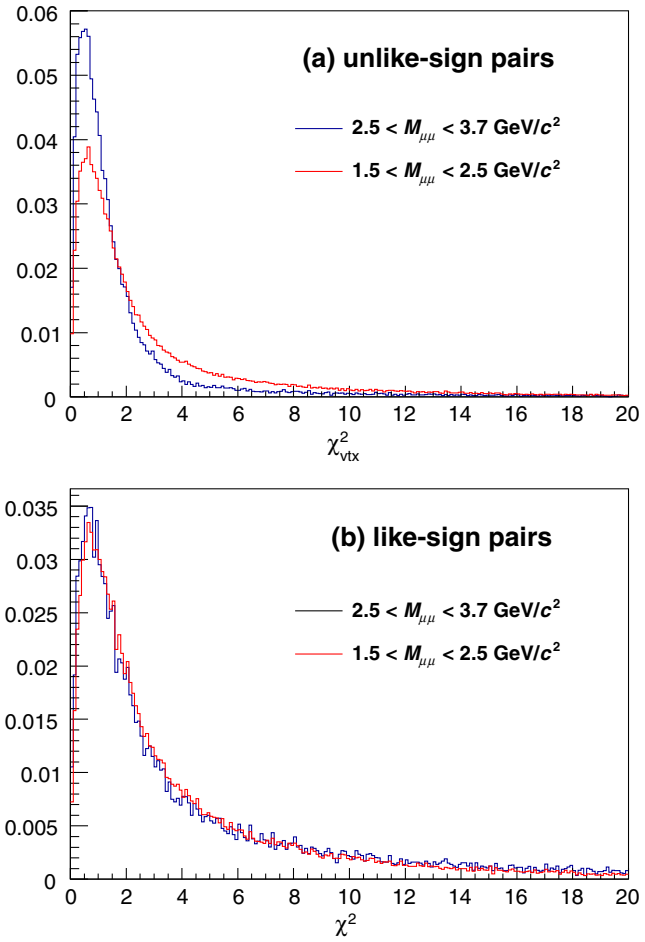

FIG. 2 (color online). The $\chi^2_{\rm vtx}$ distributions for the nonresonance mass region (red), and signal (J/ψ) mass region (blue). The unlike-sign pairs are shown in panel (a) while the like-sign pairs are shown in panel (b). In each panel, the histograms are normalized to the total number of events.

To extract the LVM signal, we first select the foreground (unlike-sign pairs with $\chi^2_{\rm vtx} < 3.6$) and a subset of unlike-sign background events by selecting pairs with $\chi^2_{\rm vtx} > 3.6$. We then renormalize this subset of background events to obtain a spectrum which represents the unlike-sign background in the foreground spectra with $\chi^2_{\rm vtx} < 3.6$. The renormalization is done using two methods: one uses unlike-sign pairs and the other uses like-sign pairs. In the first method, which uses the unlike-sign pairs, the ratio of the spectra of $\chi^2_{\rm vtx} < 3.6$ and $\chi^2_{\rm vtx} > 3.6$ pairs is fitted by a polynomial in the nonresonance region and the unlike-sign $\chi^2_{\rm vtx} > 3.6$ spectra are then multiplied by the fit function. In the second method, the ratio of the spectra of $\chi^2_{\rm vtx} < 3.6$ and $\chi^2_{\rm vtx} > 3.6$ from like-sign pairs is used directly to give the shape of the background in the resonance region but is then further multiplied by another normalization factor which accounts for small differences between the like-sign and unlike-sign distributions. This second normalization factor (C) is derived by forcing the integrated signal to be zero in the nonresonance mass range:

$$\int_{1.3}^{2.5} N^{+-}_{\chi^2<3.6}(M) - C * \int_{1.3}^{2.5} N^{+-}_{\chi^2_{\rm vtx}>3.6}(M)\left(N^{++/--}_{\chi^2_{\rm vtx}<3.6}(M)/N^{++/--}_{\chi^2_{\rm vtx}>3.6}(M)\right) = 0 \quad (1)$$

where $N^{+-}(M)$ and $N^{++/--}(M)$ are the number of unlike-sign and like-sign pairs, respectively, with the indicated $\chi^2_{\rm vtx}$ cut. Background estimates using these two methods are shown in Fig. 3. Both estimates of the background match the nonresonance region of the unlike-sign spectrum. However, because the second method includes a two-step normalization which introduces higher statistical fluctuations on the background subtraction, the second method is only used for a cross check. The insert in Fig. 3(b) shows that the acceptance and reconstruction efficiency drops quickly at low mass which explains the higher J/ψ yield compared to the low-mass vector mesons.

The unlike-sign dimuon spectra, with $\chi^2_{\rm vtx} < 3.6$, in the region of interest ($0 < M_{\mu^+\mu^-} < 2$ GeV/c^2), have contributions from three mesons, ω, ρ, and ϕ. The ϕ meson is partly resolved while ω and ρ mesons are completely merged; hence, the combined yield for ω and ρ mesons was extracted. It was found that the reconstructed mass spectra of the simulated ω and ϕ are fitted well by Gaussian distributions, while in the case of ρ, a Breit-Wigner distribution matched the mass spectrum, which motivated using these distributions to fit the invariant mass spectra.

The background-subtracted dimuon spectra in the low-mass region, $0.3 < M_{\mu^+\mu^-} < 2.5$ GeV/c^2, are fitted with two Gaussian distributions and a Breit-Wigner distribution. Note that the Breit-Wigner form is used as an empirical fit function; Γ is not meant to reflect the actual width of ρ. Other forms, such as a Gaussian distribution, were used for

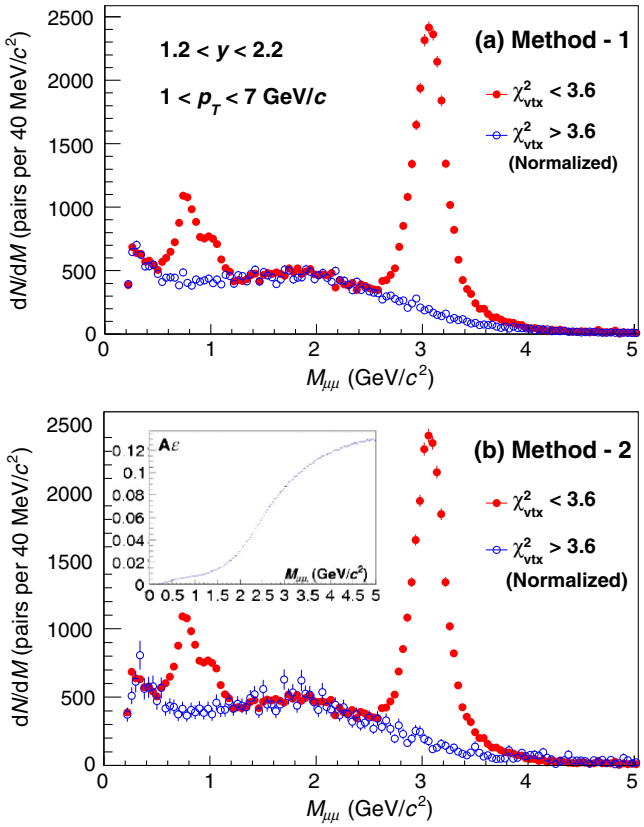

FIG. 3 (color online). The unlike-sign dimuon invariant mass spectrum (solid red points) and the background spectrum (empty blue circles) normalized using the first normalization method in panel (a), and using the second normalization method in panel (b). The insert in panel (b) shows the muon arms acceptance and reconstruction efficiency.

ρ with less than a 2% change in the yield of ϕ. The means and widths (Γ for a Breit-Wigner distribution) of the reconstructed ω, ρ and ϕ were extracted using the PHENIX simulation chain and used as a first approximation in fitting the data. The masses and widths are free parameters in the fit to account for small detector effects which result in $< 2\%$ variations with respect to the Particle Data Group values. It is important to note that the parameters from data and simulation converged to the same values within uncertainties without any systematic shifts.

To ensure the robustness of the yield extraction, an additional yield extraction procedure is employed. The background is fitted with a polynomial and the result of the fit is added to two Gaussian distributions and a Breit-Wigner distribution which are then fitted to the dimuon invariant mass spectrum while constraining the added function with the background spectra fit parameters. The background normalization is a free parameter.

Figure 4 shows an example of the different yield extraction methods. Figure 4(a) shows the unlike-sign dimuon invariant mass spectrum (solid black circles) and the background spectrum (empty blue circles), while Fig. 4(b) shows the same background spectrum fitted with a fourth-order polynomial. Figure 4(c) shows the unlike-sign dimuon invariant mass spectrum after subtracting the normalized background spectrum, shown in Fig. 4(b), fitted by two Gaussian distributions and a Breit-Wigner distribution. As a cross check, a first-order polynomial was added to the fit and the yields re-extracted and the resulting yields changed by less than 1%. Figure 4(d) shows the unlike-sign dimuon invariant mass spectrum without background subtraction fitted by two Gaussian distributions, a Breit-Wigner distribution and a fourth-order polynomial constrained from the fit results shown in Fig. 4(b). The yields extracted using the two methods illustrated in Figs. 4(c) and 4(b) gave consistent results, well within uncertainties.

The data are binned as a function of p_T over the range $1 < p_T < 7$ GeV/c for the rapidities $1.2 < |y| < 2.2$. In addition, the data integrated over the p_T range $1 < p_T < 7$ GeV/c were studied as a function of rapidity. The raw yields in this measurement were extracted using background subtraction as well as background fit methods, and in the case of the background fit, several polynomials of different orders were attempted. As an example, the invariant mass spectra are fitted by the function that includes a fourth-order polynomial, as defined below:

$$f(x) = 0.58 \times N_\omega \times BW(x, M_{\omega+\rho}, \Gamma_\rho) + \frac{N_\omega}{\sqrt{2\pi}\sigma_\omega} G(x, M_{\omega+\rho}, \sigma_\omega) + \frac{N_\phi}{\sqrt{2\pi}\sigma_\phi} G(x, M_\phi, \sigma_\phi) + pol4 \quad (2)$$

where BW and G are Breit-Wigner and Gaussian functions, respectively, and $pol4$ is a fourth-order polynomial. N_ω and N_ϕ are the yields of ω and ϕ, and $M_{\omega+\rho}$ and M_ϕ are their mean values. The fit functions of ω (Gaussian) and ρ (Breit-Wigner) are constrained to have the same mean value and the ratio of their yields, N_ρ/N_ω is set to 0.58. The factor 0.58 is the ratio of ρ and ω cross sections, $\sigma_\rho/\sigma_\omega = 1.15 \pm 0.15$ [21], multiplied by the ratio of their branching ratios [22]. As a cross check, the ratio N_ρ/N_ω was unconstrained in the fit and the yield of ϕ changed by less than 3%. The results of fitting the invariant mass spectra for different p_T bins at $1.2 < y < 2.2$ are listed in Table I.

The extracted yields of $\omega + \rho$ and ϕ were consistent among all fits. Therefore, the yields and the uncertainties of the fit with the best χ^2 are used in the differential cross section calculations. The variations among the yields of the fit with the best χ^2 and those of the other fits are considered as systematic uncertainties on the yield extraction.

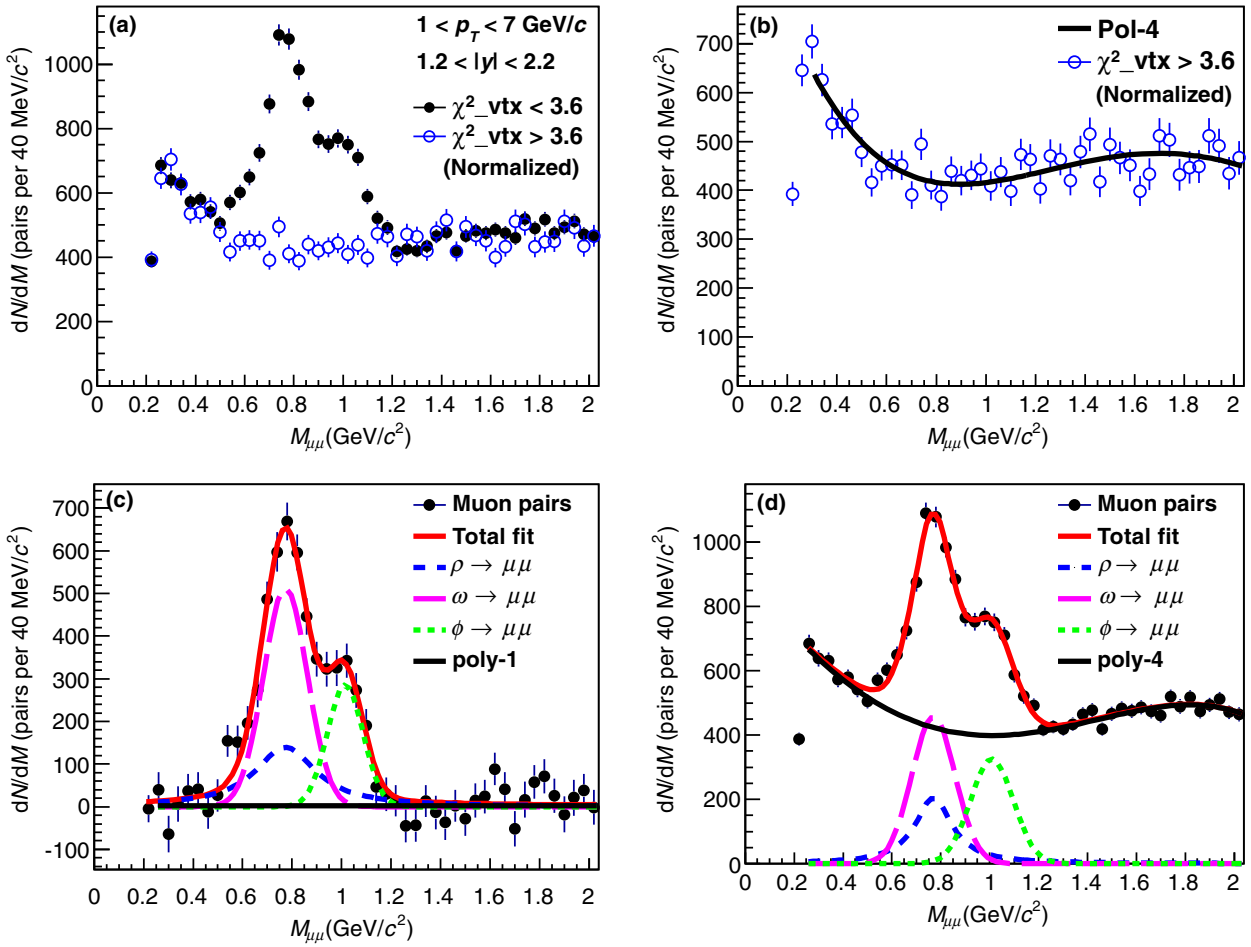

FIG. 4 (color online). Raw unlike-sign dimuon spectra (solid black circles) along with normalized background (empty blue circles) separated by $\chi^2_{\mathrm{vtx,cut}}$ in panel (a). Panel (b) shows the normalized background spectrum fitted with a fourth-order polynomial. Panels (c) and (d) show the fitted spectra with (left) and without (right) background subtraction.

The acceptance and reconstruction efficiency ($A\varepsilon_{\mathrm{rec}}$) of the muon spectrometers, including the MuID trigger efficiency, is determined by individually running PYTHIA 6.421 (Default) [23] generated ω, ρ, and ϕ through a full GEANT simulation of the PHENIX detector. The simulated vertex distribution was tuned to match that of the 2009 data. The simulated events are reconstructed in the same manner as the data and the same cuts are applied as in the real data analysis.

TABLE I. The results of fitting the foreground spectrum by a function that includes two Gaussian distributions, a Breit-Wigner distribution and a fourth-order polynomial, over the mass range $0.3 < M_{\mu\mu} < 2.0$ GeV/c^2 for the listed p_T bins.

p_T(GeV/c)	1.0–2.0	2.0–2.5	2.5–3.0	3.0–4.5	4.5–7.0
N_ω	$(68 \pm 5) \times 10^1$	$(63 \pm 8) \times 10^1$	$(39 \pm 4) \times 10^1$	$(36 \pm 5) \times 10^1$	$(4.8 \pm 1.2) \times 10^1$
$M_{\omega+\rho}$ (GeV/c^2)	$(77 \pm 1) \times 10^{-2}$	$(77 \pm 1) \times 10^{-2}$	$(77 \pm 1) \times 10^{-2}$	$(76 \pm 1) \times 10^{-2}$	$(80 \pm 2) \times 10^{-2}$
Γ_ρ(GeV/c^2)	$(18 \pm 4) \times 10^{-2}$	$(22 \pm 4) \times 10^{-2}$	$(22 \pm 2) \times 10^{-2}$	$(18 \pm 4) \times 10^{-2}$	$(19 \pm 2) \times 10^{-2}$
σ_ω(GeV/c^2)	$(8.8 \pm 1.3) \times 10^{-2}$	$(85 \pm 8) \times 10^{-3}$	$(8.8 \pm 1.2) \times 10^{-2}$	$(8.1 \pm 1.3) \times 10^{-2}$	$(7.2 \pm 1.6) \times 10^{-2}$
N_ϕ	$(39 \pm 8) \times 10^1$	$(53 \pm 6) \times 10^1$	$(32 \pm 4) \times 10^1$	$(28 \pm 3) \times 10^1$	38 ± 10
M_ϕ (GeV/c^2)	$(100 \pm 1) \times 10^{-2}$	$(99 \pm 1) \times 10^{-2}$	$(100 \pm 1) \times 10^{-2}$	$(100 \pm 2) \times 10^{-2}$	$(106 \pm 6) \times 10^{-2}$
σ_ϕ(GeV/c^2)	$(7.5 \pm 1.4) \times 10^{-2}$	$(8.8 \pm 1.3) \times 10^{-2}$	$(8.8 \pm 1.1) \times 10^{-2}$	$(8.8 \pm 1.0) \times 10^{-2}$	$(7.2 \pm 1.1) \times 10^{-2}$
p0	$(20 \pm 4) \times 10^1$	$(5.9 \pm 3.8) \times 10^1$	$(13 \pm 3) \times 10^1$	$(9.5 \pm 2.8) \times 10^1$	8.6 ± 1.3
p1	$(-3.8 \pm 2.0) \times 10^2$	$(3.0 \pm 1.8) \times 10^2$	$(-2.5 \pm 1.3) \times 10^2$	$(-1.8 \pm 1.3) \times 10^2$	-15 ± 2.2
p2	$(6.2 \pm 3.1) \times 10^2$	$(-4.9 \pm 2.5) \times 10^2$	$(3.4 \pm 1.8) \times 10^2$	$(2.2 \pm 1.8) \times 10^2$	39 ± 1.5
p3	$(-3.6 \pm 2.0) \times 10^2$	$(2.6 \pm 1.4) \times 10^2$	$(-2.1 \pm 1.0) \times 10^2$	$(-1.3 \pm 1.0) \times 10^2$	-35 ± 1
p4	$(6.7 \pm 4.3) \times 10^1$	$(-4.7 \pm 2.9) \times 10^1$	$(4.6 \pm 2.1) \times 10^1$	$(2.6 \pm 2.1) \times 10^1$	9.2 ± 0.4
χ^2/d.o.f	43.2/33	28.1/33	24.7/33	29.2/33	39.7/33

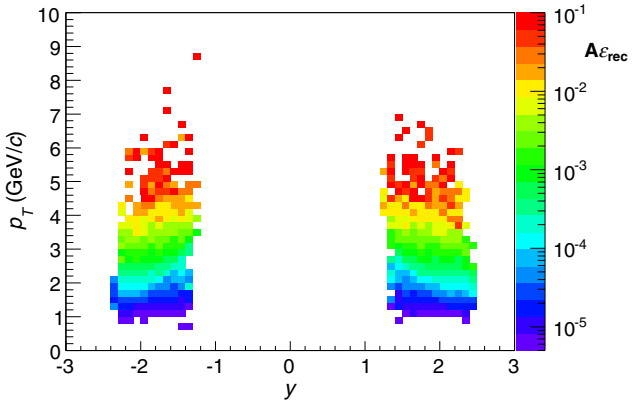

FIG. 5 (color online). The $A\varepsilon_{\rm rec}$ as a function of rapidity (x axis) and p_T (y axis) for ω.

The p_T and rapidity distributions of the generated events match the measured ones very well. The insert in Fig. 3 shows the $A\varepsilon_{\rm rec}$ as a function of invariant mass, while Fig. 5 shows the $A\varepsilon_{\rm rec}$ as a function of p_T and rapidity for ω, as an example; the $A\varepsilon_{\rm rec}$ for ρ and ϕ look very similar. The p_T-dependent $A\varepsilon_{\rm rec}$ drops quickly at lower p_T which is the reason for limiting this study to $p_T > 1$ GeV/c.

IV. RESULTS

The differential cross section is evaluated according to the following relation:

$$BR\frac{d^2\sigma}{dydp_T} = \frac{1}{\Delta y \Delta p_T}\frac{N}{A\varepsilon_{\rm rec}\varepsilon_{\rm BBC}}\frac{\sigma_{\rm BBC}}{N_{\rm MB}^{\rm BBC}} \qquad (3)$$

where $\sigma_{\rm BBC}$ is the PHENIX BBC sampled cross section, 23.0 ± 2.2 mb at $\sqrt{s} = 200$ GeV, which is determined from the van der Meer scan technique [24]. BR is the branching ratio to dimuons [$BR(\omega \to \mu\mu) = (9.0 \pm 3.1) \times 10^{-5}$, $BR(\rho \to \mu\mu) = (4.55 \pm 0.28) \times 10^{-5}$, and $BR(\phi \to \mu\mu) = (2.87 \pm 0.19) \times 10^{-4}$] [22]. $\varepsilon_{\rm BBC} = 0.795 \pm 0.02$, is the BBC efficiency for hard scattering events [25]. $N_{\rm MB}^{\rm BBC}$ is the number of MB events, and N is the number of the observed mesons. In the p_T-dependent study, the LVM yields were extracted for each arm separately and the weighted average of the two arms was used in the differential cross section calculations. $A\varepsilon_{\rm rec}$ is the acceptance and reconstruction efficiency.

The ω and ρ yields are measured together and the p_T-dependent and rapidity-dependent differential cross sections are reported as $BR(\omega \to \mu\mu) \times d^2\sigma/dydp_T(\omega) + BR(\rho \to \mu\mu) \times d^2\sigma/dydp_T(\rho)$ and $BR(\omega \to \mu\mu) \times d\sigma/dy(\omega) + BR(\rho \to \mu\mu) \times d\sigma/dy(\rho)$, respectively, to minimize the contribution of uncertainties from branching ratios and total cross sections needed to calculate the absolute $(\omega + \rho)$ differential cross section. The $A\varepsilon_{\rm rec}$ for $\omega + \rho$ is taken as the weighted average of the individual $A\varepsilon_{\rm rec}$, where the averaging is done based on ω and ρ branching ratios.

The systematic uncertainties associated with this measurement can be divided into three categories based upon the effect each source has on the measured results. All uncertainties are reported as standard deviations. Type-A: point-to-point uncorrelated uncertainties allow the data points to move independently with respect to one another and are added in quadrature with statistical uncertainties, and include a 3% signal extraction uncertainty. The 3% signal extraction uncertainty is the average variation between the results from the different yield extraction fits. Type-B: point-to-point correlated uncertainties allow the data points to move coherently together, though not by a simple single multiplicative factor. These systematic uncertainties include a 4% uncertainty from MuID tube efficiency and 2% from MuTr overall efficiency. An 8% uncertainty on the yield is assigned to account for a 2% absolute momentum-scale uncertainty, which was estimated by measuring the J/ψ mass. A 9% (7%) uncertainty is assigned to the $-2.2 < y < -1.2 (1.2 < y < 2.2)$ rapidity due to the uncertainties in the $A\varepsilon_{\rm rec}$ determination method itself. The $A\varepsilon_{\rm rec}$ at the lowest-p_T bin is small, as shown in Fig. 5, and sensitive to variations in the slope of the input p_T distribution which affects the differential cross section calculations at this p_T bin. To understand this effect, the p_T-dependent cross section is fitted by three commonly used fit functions (Hagedorn [26], Kaplan [27], and Tsallis [2]) over the p_T range, $2 < p_T < 7$ GeV/c, and the fitted functions are extrapolated to the lowest-p_T bin, $1 < p_T < 2$ GeV/c. The differences between the values extracted from these fits and the measured one at the lowest-p_T bin is within 8%, and hence a 8% systematic uncertainty is assigned to the lowest-p_T bin to account for these differences. For the integrated and rapidity-dependent cross sections the 8% uncertainty is assigned to all data bins because the lowest-p_T bin is dominant. Type-B systematic uncertainties are added in quadrature and are shown as shaded bands on the associated data points. Finally, type-C: an overall normalization uncertainty of 10% was assigned for the BBC cross section and efficiency uncertainties, which allow the data points to move together by a common multiplicative factor. These systematic uncertainties are listed in Table II.

The open charm contribution to the signal is a possible source of systematic uncertainty. Even though the background-subtracted dimuon spectrum in Fig. 4(c) shows no evidence of a remaining background, a Monte Carlo simulation was carried out to verify that the open charm contribution to the signal is negligible after background subtraction. A single-particle PYTHIA simulation of open charm was generated and run through the PHENIX simulation chain. The charm differential cross section at forward rapidity, $d\sigma_{c\bar{c}}/dy|_{y=1.6} = 0.243 \pm 0.013(\text{stat}) \pm 0.105(\text{data syst})^{+0.049}_{-0.087}$ (PYTHIA syst) mb [28], is used with

TABLE II. Systematic uncertainties included in the invariant yield and differential cross section calculations, where S (N) is for the $-2.2 < y < -1.2 (1.2 < y < 2.2)$ rapidity. As explained in the text, there is a 8% type-B systematic uncertainty due to small acceptance that impacts the low-p_T region only which is not listed below.

Type	Origin	Value (S/N)
A	Signal extraction	3%
B	MuID efficiency	4%
B	MuTr efficiency	2%
B	$A\varepsilon_{\rm rec}$	9%/7%
B	Absolute momentum scale	8%
Total	Quadratic sum of (B)	13%/12%
C	BBC efficiency (Global)	10%

an inclusive branching ratio, $BR(D \to \mu + X) = 0.176$ [22]. The simulated events were then reconstructed using identical code to that used in the real data analysis, and after applying all cuts used in the analysis, the surviving rate of open charm was negligible in comparison to the low-mass vector-meson yields. Additionally, a similar study of the η and ω Dalitz decays showed that they were negligible.

The differential cross sections for $\omega + \rho$ and ϕ as a function of p_T are shown in Figs. 6 and 7, respectively, and listed in Table III. The appropriate p_T value where each point was plotted is chosen such that the fit function, a function selected to fit the p_T distribution, is equal to its mean value [29]. The results are listed in the first column in Table III. Figures 6 and 7 also include some standard tunes of PYTHIA (ATLAS-CSC [30], default [23] and

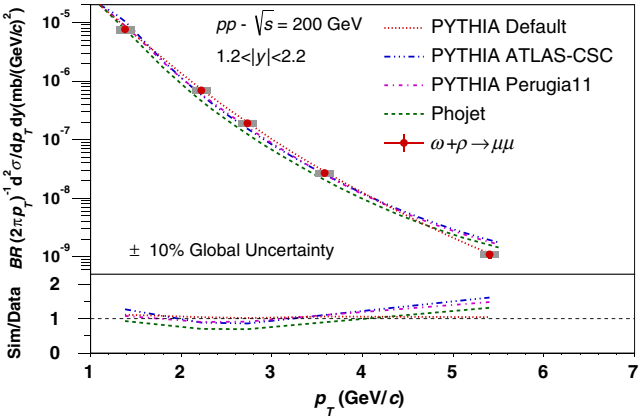

FIG. 6 (color online). (Top) p_T-dependent differential cross section vs p_T of $\omega + \rho$ at rapidity, $1.2 < |y| < 2.2$. The error bars represent the statistical uncertainties, and the gray shaded band represents the quadratic sum of type-B systematic uncertainties. The data are compared with the PYTHIA ATLAS-CSC, default and PRUGIA-11 tunes and PHOJET. (Bottom) Ratio between data and models.

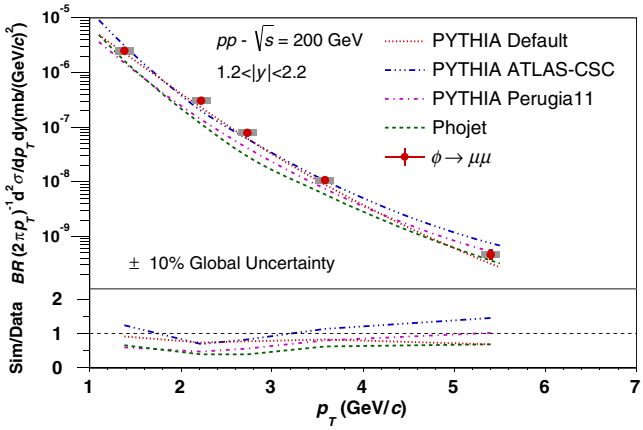

FIG. 7 (color online). (Top) p_T-dependent differential cross section vs p_T of ϕ at rapidity, $1.2 < |y| < 2.2$. The error bars represent the statistical uncertainties, and the gray shaded band represents the quadratic sum of type-B systematic uncertainties. The data are compared with the PYTHIA ATLAS-CSC, default and PERUGIA-11 tunes and PHOJET. (Bottom) Ratio between data and models.

PERUGIA-11 [31]) and PHOJET [32]. The bottom panels in Figs. 6 and 7 show the ratio between the measurement and the model predictions. The default PYTHIA tune was based on e^+e^- and $p\bar{p}$ data and we used CTEQ5L parton distribution functions. The PERUGIA-11 tune takes into account the MB and underlying-event data at $\sqrt{s} = 0.9$ and 7 TeV from the Large Hadron Collider and the ATLAS-CSC was tuned on the Tevatron data for $p\bar{p}$ collisions at $\sqrt{s} = 1.8$ TeV. In addition, the transverse distribution for the partons in the proton is described by a double-Gaussian in the ATLAS-CSC tune while PERUGIA-11 uses a smoother proton form factor which decreases the multiplicity fluctuations. The PHOJET model investigates photon-photon collisions in the framework of the two-component dual parton model. The model contains contributions from direct, resolved soft and hard interactions. However, it only includes leading-order QCD processes (no W/Z, etc.) and neither heavy-quark production nor dedicated high-p_T physics options.

These model predictions were also tested against previously published midrapidity data [2] as shown in Figs. 8 and 9. PYTHIA ATLAS-CSC and PERUGIA-11 tunes reproduce the differential cross section at both midrapidity and forward rapidity for ω and $\omega + \rho$, respectively, while PHOJET under predicts the data in both cases. The PYTHIA ATLAS-CSC tune reproduces the ϕ differential cross sections at forward rapidities. The PYTHIA ATLAS-CSC and PERUGIA-11 tunes and PHOJET fail to match the data below 1 GeV/c. Generally, PYTHIA and PHOJET seem to do a better job reproducing $\omega + \rho$ than ϕ.

Figure 10 and Table IV show the differential cross section as a function of rapidity for $\omega + \rho$ in Fig. 10(a) and ϕ in Fig. 10(b), along with PYTHIA tunes (ATLAS-CSC,

TABLE III. Differential cross sections in $b/(\mathrm{GeV}/c)$ and p_T in (GeV/c) of $\omega+\rho$ and ϕ at $1.2<|y|<2.2$ with statistical and type-A systematic uncertainties added in quadrature and type-B systematic uncertainties.

p_T	$\frac{BR}{2\pi p_T}\frac{d^2\sigma_{\omega+\rho\to\mu\mu}}{dydp_T}$	$\frac{BR}{2\pi p_T}\frac{d^2\sigma_{\phi\to\mu\mu}}{dydp_T}$
(GeV/c)	$[b/(\mathrm{GeV}/c)^2]$	$[b/(\mathrm{GeV}/c)^2]$
1.38	$(8.41\pm0.67\pm1.26)\times10^{-09}$	$(2.76\pm0.35\pm0.41)\times10^{-09}$
2.17	$(7.19\pm0.71\pm0.93)\times10^{-10}$	$(3.19\pm0.36\pm0.41)\times10^{-10}$
2.65	$(1.95\pm0.19\pm0.25)\times10^{-10}$	$(8.16\pm0.93\pm1.06)\times10^{-11}$
3.58	$(2.68\pm0.29\pm0.35)\times10^{-11}$	$(1.09\pm0.14\pm0.14)\times10^{-11}$
5.40	$(1.10\pm0.16\pm0.14)\times10^{-12}$	$(4.71\pm0.90\pm0.61)\times10^{-13}$

default, and PERUGIA-11) and PHOJET. It can be seen in Fig. 10 that default and PERUGIA-11 tunes reproduce the $\omega+\rho$ results, while the ATLAS-CSC tune matches the ϕ forward-rapidity results.

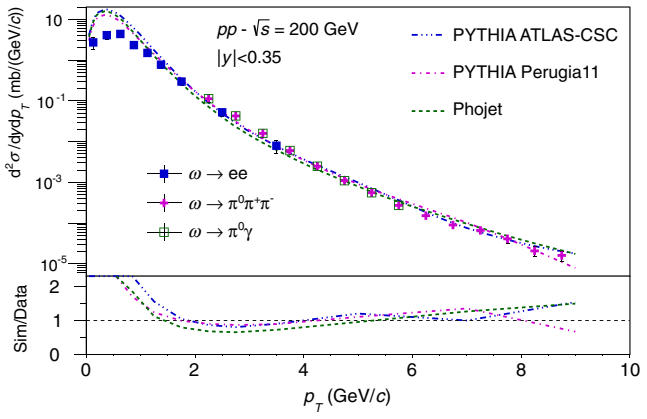

FIG. 8 (color online). (Top) p_T-dependent differential cross sections of ω at rapidity, $|y|<0.35$ [2]. The data are compared with the PYTHIA ATLAS-CSC, default and PERUGIA-11 tunes and PHOJET. (Bottom) Ratio between data and models.

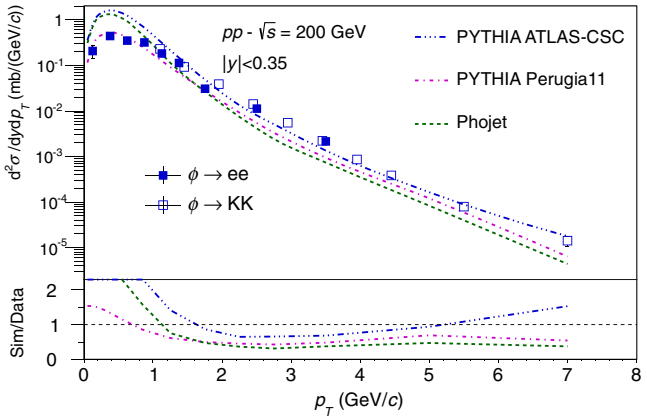

FIG. 9 (color online). (Top) p_T-dependent differential cross sections of ϕ at rapidity, $|y|<0.35$ [2]. The data are compared with the PYTHIA ATLAS-CSC, default and PERUGIA-11 tunes and PHOJET. (Bottom) Ratio between data and models.

The acceptance at low p_T is very small in the low-mass region which prevents us from extracting the differential cross sections, $d\sigma/dy$, summed over all p_T directly from the data. Instead, we report $d\sigma/dy$ integrated over the measured

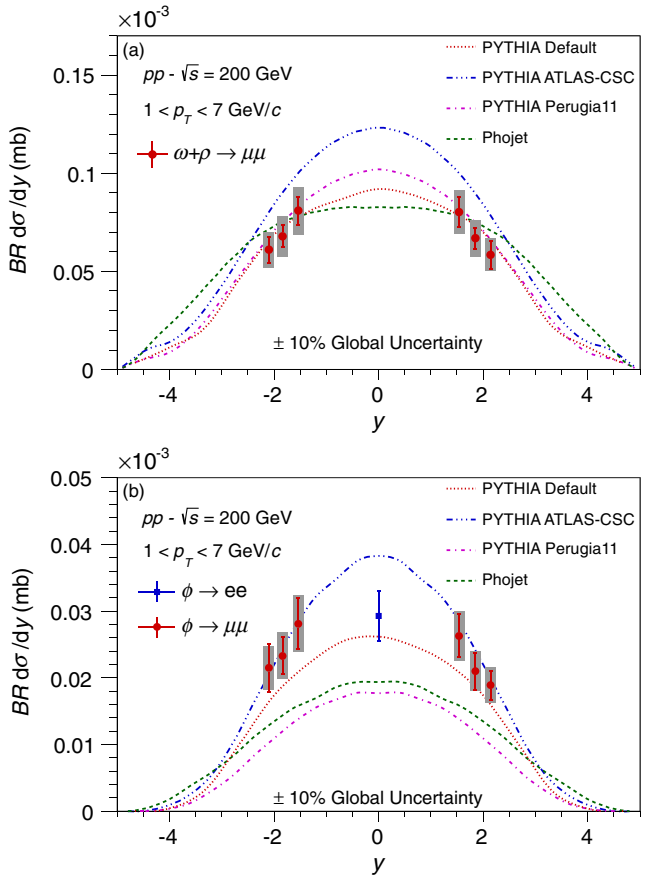

FIG. 10 (color online). Rapidity dependent differential cross section of $\omega+\rho$ (a) and ϕ (b) along with previous PHENIX results [2] summed over the p_T range, $1<p_T<7$ GeV. The error bars represent the quadratic sum of the statistical uncertainties and type-A systematic uncertainties, and the gray shaded band represents the quadratic sum of type-B systematic uncertainties. The data are compared with the PYTHIA ATLAS-CSC and PERUGIA-11 tunes and PHOJET.

TABLE IV. Differential cross sections in b and rapidity of $\omega + \rho$ and ϕ at $1 < p_T < 7$ GeV/c with statistical and type-A systematic uncertainties added in quadrature and type-B systematic uncertainties.

y	$BR\frac{d\sigma_{\omega+\rho\to\mu\mu}}{dy}$ (nb)	$BR\frac{d\sigma_{\phi\to\mu\mu}}{dy}$ (nb)
−2.10	$61.1 \pm 6.7 \pm 9.2$	$21.5 \pm 3.7 \pm 3.2$
−1.84	$67.9 \pm 5.6 \pm 10.2$	$23.3 \pm 2.8 \pm 3.5$
−1.54	$81.0 \pm 7.1 \pm 12.2$	$28.1 \pm 3.8 \pm 4.2$
1.54	$80.3 \pm 7.6 \pm 11.2$	$26.3 \pm 3.2 \pm 3.7$
1.85	$66.9 \pm 5.4 \pm 9.4$	$21.0 \pm 2.8 \pm 2.9$
2.14	$58.4 \pm 7.4 \pm 8.2$	$18.9 \pm 2.2 \pm 2.6$

p_T range, $d\sigma/dy(\omega+\rho\to\mu\mu)(1<p_T<7\text{GeV}/c, 1.2<|y|<2.2) = 80\pm6(\text{stat})\pm12(\text{syst})\text{nb}$ and $d\sigma/dy(\phi\to\mu\mu)(1<p_T<7\,\text{GeV}/c, 1.2<|y|<2.2) = 27\pm3(\text{stat})\pm4(\text{syst})\,\text{nb}$.

The ratio $N_\phi/(N_\omega+N_\rho) = BR(\phi\to\mu\mu)\sigma_\phi/(BR(\omega\to\mu\mu)\sigma_\omega + BR(\rho\to\mu\mu)\sigma_\rho)$, corrected for acceptance and efficiency, was determined for $1<p_T<7\,\text{GeV}/c$ and $1.2<|y|<2.2$, giving $0.390\pm0.021(\text{stat})\pm0.035(\text{syst})$, as shown in Fig. 11 and listed in Table V. Systematic uncertainties including MuID and MuTr efficiencies, absolute momentum scale and BBC efficiency cancel out when taking the yield ratio.

Figure 11 also shows PYTHIA (ATLAS-CSC, default, and PERUGIA-11 tunes) and PHOJET. The ATLAS-CSC tune reproduces the ratio while the other models underestimate it. The ALICE experiment also measured this ratio in $p+p$ collisions at $\sqrt{s} = 7$ TeV in the dimuon rapidity region $2.5 < y < 4$. The reported value is $0.416 \pm 0.032(\text{stat}) \pm 0.004(\text{syst})$ [5] over the p_T range $1 < p_T < 5$ which is consistent with our result.

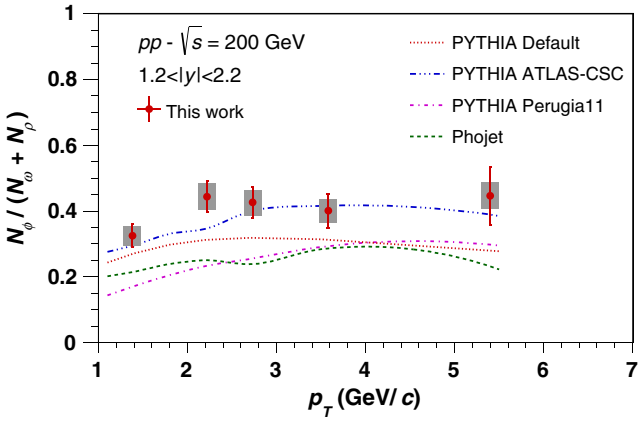

FIG. 11 (color online). $N_\phi/(N_\omega+N_\rho)$ as a function of p_T. The error bars represent the quadratic sum of the statistical uncertainties and type-A systematic uncertainties, and the gray shaded band represents the quadratic sum of type-B systematic uncertainties.

TABLE V. $N_\phi/(N_\omega+N_\rho)$ and p_T in (GeV/c) with statistical and type-A systematic uncertainties added in quadrature and type-B systematic uncertainties.

p_T(GeV/c)	$N_\phi/(N_\omega+N_\rho)$
1.38	$0.33 \pm 0.04 \pm 0.03$
2.17	$0.44 \pm 0.05 \pm 0.04$
2.65	$0.43 \pm 0.05 \pm 0.04$
3.58	$0.40 \pm 0.05 \pm 0.04$
5.40	$0.45 \pm 0.09 \pm 0.04$

V. SUMMARY AND CONCLUSIONS

In summary, we studied the low-mass vector-meson, ω, ρ, and ϕ, production in $p+p$ collisions at $\sqrt{s} = 200$ GeV for $1.2 < |y| < 2.2$ and $1.0 < p_T < 7.0$ GeV/c, through the dimuon decay channel. We measured $\omega+\rho$, and ϕ differential cross sections as a function of p_T as well as a function of rapidity.

The differential cross sections, $d\sigma/dy$ of $\omega+\rho$ and ϕ, were evaluated over the measured p_T range, $d\sigma/dy(\omega+\rho\to\mu\mu)(1<p_T<7\,\text{GeV}/c, 1.2<|y|<2.2) = 80\pm6(\text{stat})\pm12(\text{syst})\,\text{nb}$ and $d\sigma/dy(\phi\to\mu\mu)(1<p_T<7\,\text{GeV}/c, 1.2<|y|<2.2) = 27\pm3(\text{stat})\pm4(\text{syst})\,\text{nb}$. The ratio $N_\phi/(N_\omega+N_\rho)$, at $1<p_T<7$ GeV/c and $1.2<|y|<2.2$, was also determined, and is $0.390\pm0.021(\text{stat})\pm0.035(\text{syst})$, which is consistent with the ALICE measurement at larger rapidity and higher energy. This agreement with the ALICE result at $N_\phi/(N_\omega+N_\rho)\sim0.4$, which is higher than PYTHIA default at ~0.3, suggests a higher $g+g$ contribution to ϕ production.

The data were compared to some commonly used PYTHIA tunes and PHOJET. Overall, the PYTHIA ATLAS-CSC and default tunes describe forward rapidity data except for the ϕ rapidity distribution and describe mid-rapidity data above 1 GeV/c. The PYTHIA PERUGIA-11 tune describes the $\omega+\rho$ differential cross section while it underestimates the ϕ differential cross section. Generally, all these leading-order perturbative QCD-based event generators successfully describe the shape of the LVM p_T distribution.

ACKNOWLEDGMENTS

We thank the staff of the Collider-Accelerator and Physics Departments at Brookhaven National Laboratory and the staff of the other PHENIX participating institutions for their vital contributions. We acknowledge support from the Office of Nuclear Physics in the Office of Science of the Department of Energy, the National Science Foundation, Abilene Christian University Research Council, the Research Foundation of SUNY, and the Dean of the College of Arts and Sciences, Vanderbilt University (USA), the Ministry of Education, Culture, Sports, Science, and Technology and the Japan Society for the Promotion of Science (Japan), the Conselho Nacional de

Desenvolvimento Científico e Tecnológico and Fundação de Amparo à Pesquisa do Estado de São Paulo (Brazil), the Natural Science Foundation of China (People's Republic of China), the Ministry of Science, Education, and Sports (Croatia), the Ministry of Education, Youth and Sports (Czech Republic), the Centre National de la Recherche Scientifique, Commissariat à l'Énergie Atomique, and Institut National de Physique Nucléaire et de Physique des Particules (France), the Bundesministerium für Bildung und Forschung, Deutscher Akademischer Austausch Dienst, and Alexander von Humboldt Stiftung (Germany), the OTKA NK 101 428 grant and the Ch. Simonyi Fund (Hungary), he Department of Atomic Energy and Department of Science and Technology (India), the Israel Science Foundation (Israel), he Basic Science Research Program through NRF of the Ministry of Education (Korea), the Physics Department, Lahore University of Management Sciences (Pakistan), the Ministry of Education and Science, the Russian Academy of Sciences, the Federal Agency of Atomic Energy (Russia), the VR and Wallenberg Foundation (Sweden), the U.S. Civilian Research and Development Foundation for the Independent States of the Former Soviet Union, the Hungarian American Enterprise Scholarship Fund, and the US-Israel Binational Science Foundation.

[1] B. Abelev *et al.* (STAR Collaboration), Phys. Rev. C **79**, 064903 (2009).
[2] A. Adare *et al.* (PHENIX Collaboration), Phys. Rev. D **83**, 052004 (2011).
[3] T. Alexopoulos *et al.* (E735 Collaboration), Z. Phys. C **67**, 411 (1995).
[4] B. Abelev *et al.* (ALICE Collaboration), Eur. Phys. J. C **72**, 2183 (2012).
[5] B. Abelev *et al.* (ALICE Collaboration), Phys. Lett. B **710**, 557 (2012).
[6] R. Aaij *et al.* (LHCb Collaboration), Phys. Lett. B **703**, 267 (2011).
[7] P. Koch, B. Müller, and J. Rafelski, Phys. Rep. **142**, 167 (1986).
[8] C. Alt *et al.* (NA49 Collaboration), Phys. Rev. C **78**, 044907 (2008).
[9] B. Alessandro *et al.* (NA50 Collaboration), Phys. Lett. B **555**, 147 (2003).
[10] D. Adamová *et al.* (CERES Collaboration), Phys. Rev. Lett. **96**, 152301 (2006).
[11] R. Arnaldi *et al.* (NA60 Collaboration), Phys. Lett. B **699**, 325 (2011).
[12] A. Adare *et al.* (PHENIX Collaboration), Phys. Rev. C **83**, 024909 (2011).
[13] B. Abelev *et al.* (STAR Collaboration), Phys. Lett. B **673**, 183 (2009).
[14] H. van Hees and R. Rapp, Nucl. Phys. **A806**, 339 (2008).
[15] D. Adamová *et al.* (CERES Collaboration), Phys. Lett. B **666**, 425 (2008).
[16] R. Arnaldi *et al.* (NA60 Collaboration), Phys. Rev. Lett. **96**, 162302 (2006).
[17] K. Adcox *et al.* (PHENIX Collaboration), Nucl. Instrum. Methods Phys. Res., Sect. A **499**, 469 (2003).
[18] S. Aronson *et al.* (PHENIX Collaboration), Nucl. Instrum. Methods Phys. Res., Sect. A **499**, 480 (2003).
[19] A. Adare *et al.* (PHENIX Collaboration), Phys. Rev. C **84**, 054912 (2011).
[20] A. Adare *et al.* (PHENIX Collaboration), Phys. Rev. C **87**, 034904 (2013).
[21] A. Adare *et al.* (PHENIX Collaboration), Phys. Rev. C **81**, 034911 (2010).
[22] J. Beringer *et al.* (Particle Data Group), Phys. Rev. D **86**, 010001 (2012).
[23] T. Sjöstrand, P. Edén, C. Friberg, L. Lönnblad, G. Miu, S. Mrenna, and E. Norrbin, Comput. Phys. Commun. **135**, 238 (2001).
[24] A. Adare *et al.* (PHENIX Collaboration), Phys. Rev. D **79**, 012003 (2009).
[25] S. S. Adler *et al.* (PHENIX Collaboration), Phys. Rev. Lett. **92**, 051802 (2004).
[26] R. Hagedorn, Suppl. Al Nuovo Cimento **3**, 147 (1965).
[27] D. M. Kaplan *et al.*, Phys. Rev. Lett. **40**, 435 (1978).
[28] S. S. Adler *et al.* (PHENIX Collaboration), Phys. Rev. D **76**, 092002 (2007).
[29] G. D. Lafferty and T. R. Wyatt, Nucl. Instrum. Methods Phys. Res., Sect. A **355**, 541 (1995).
[30] C. Buttar *et al.*, Acta Phys. Pol. B **35**, 433 (2004).
[31] P. Z. Skands, Phys. Rev. D **82**, 074018 (2010).
[32] R. Engel and J. Ranft, Phys. Rev. D **54**, 4244 (1996).